

Synthesis and Properties of Charge-Ordered Thallium Halide Perovskites, $\text{CsTl}^+_{0.5}\text{Tl}^{3+}_{0.5}\text{X}_3$ ($\text{X} = \text{F}$ or Cl): Theoretical Precursors for Superconductivity?

M. Retuerto,[†] T. Emge,[†] J. Hadermann,[‡] P. W. Stephens,[§] M. R. Li,[†] Z. P. Yin,^{||} M. Croft,^{||} A. Ignatov,^{||} S. J. Zhang,[⊥] Z. Yuan,[⊥] C. Jin,[⊥] J. W. Simonson,[§] M. C. Aronson,^{§,@} A. Pan,[#] D. N. Basov,[#] G. Kotliar,^{||} and M. Greenblatt^{*,†}

[†]Department of Chemistry and Chemical Biology, Rutgers, The State University of New Jersey, 610 Taylor Road, Piscataway, New Jersey 08854, United States

[‡]EMAT, Department of Physics, University of Antwerp, Groenenborgerlaan 171, 2020 Antwerp, Belgium

[§]Department of Physics and Astronomy, The State University of New York, Stony Brook, New York 11794, United States

^{||}Department of Physics and Astronomy, Rutgers, The State University of New Jersey, 136 Frelinghuysen Road, Piscataway, New Jersey 08854, United States

[⊥]Institute of Physics, Chinese Academy of Sciences, Number 8, Zhongguancun South Street 3, Beijing 100190, China

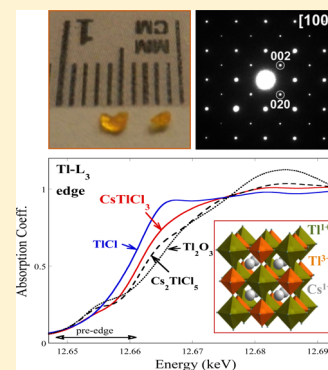
[@]Brookhaven National Laboratory, Upton, New York 11973, United States

[#]Department of Physics, University of California, San Diego, La Jolla, California 92093-0319, United States

Supporting Information

ABSTRACT: Recently, CsTlCl_3 and CsTlF_3 perovskites were theoretically predicted to be potential superconductors if they were optimally doped. The syntheses of these two compounds together with a complete characterization of the samples are reported. CsTlCl_3 was obtained as orange crystals in two different polymorphs: a tetragonal phase ($I4/m$) and a cubic phase ($Fm\bar{3}m$). CsTlF_3 was formed as a light brown powder, and also as a double cubic perovskite ($Fm\bar{3}m$). In all three CsTlX_3 phases, Tl^+ and Tl^{3+} were located in two different crystallographic positions that accommodate their different bond lengths. In CsTlCl_3 , some Tl vacancies were found in the Tl^+ position. The charge ordering between Tl^+ and Tl^{3+} was confirmed by X-ray absorption and Raman spectroscopy. The Raman spectroscopy of CsTlCl_3 at high pressure (58 GPa) did not indicate any phase transition to a possible single Tl^{2+} state. However, the highly insulating material became less resistive with an increasing high pressure, while it underwent a change in its optical properties, from transparent to deeply opaque red, indicative of a decrease in the magnitude of the band gap. The theoretical design and experimental validation of the existence of CsTlF_3 and CsTlCl_3 cubic perovskites are the necessary first steps in confirming the theoretical prediction of superconductivity in these materials.

KEYWORDS: superconductivity, mixed valence, charge order, CsTlCl_3 , CsTlF_3 , CsAuCl_3 , BaBiO_3



INTRODUCTION

The discovery of high- T_C superconductivity in mixed-valent systems such as $\text{La}_{2-x}\text{Ba}_x\text{CuO}_4$ and $\text{Ba}_{1-x}\text{K}_x\text{BiO}_3$ ^{1–4} has attracted great interest in the search for new superconducting materials, in particular, in compounds with perovskite-type structure. BaBiO_3 becomes superconducting when it is doped as $\text{Ba}_{1-x}\text{K}_x\text{BiO}_3$ ($x \sim 0.4$) and $\text{BaBi}_{1-x}\text{Pb}_x\text{O}_3$ ($x \sim 0.3$).^{4,5} In the parent compound BaBiO_3 , formally Bi^{4+} disproportionates into Bi^{3+} (lone pair $6s^2$) and Bi^{5+} ($6s^0$), which are found at alternating B sites, generating distortions from the ideal perovskite structure. Because the $6s$ orbital has a large radial extension, the $\text{Bi}-\text{O}$ bond distance is longer for the $\text{Bi}^{3+}-\text{O}$ species than for the $\text{Bi}^{5+}-\text{O}$ species.⁶ In $\text{Ba}_{1-x}\text{K}_x\text{BiO}_3$, the difference between the two $\text{Bi}-\text{O}$ bond lengths decreases and superconductivity emerges at the critical x , when the structural

distortions are completely suppressed.⁷ These observations suggest that superconductivity in the BaBiO_3 system is mediated by the same mechanism that is responsible for the charge disproportionation. However, superconductivity has not been found in other similar mixed-valent systems. For example, compounds CsAuX_3 ($\text{X} = \text{Cl}$, Br , or I) with Au^+ and Au^{3+} mixed-valent states^{8–10} and exactly one hole per site are semiconductors (at low pressure) with a large band gap. Although the conductivity of CsAuX_3 increases several orders of magnitude at high pressures, superconductivity has not been found thus far.^{11–13} In CsAuX_3 , at ambient pressure, the

Received: July 18, 2013

Revised: September 17, 2013

Published: September 18, 2013

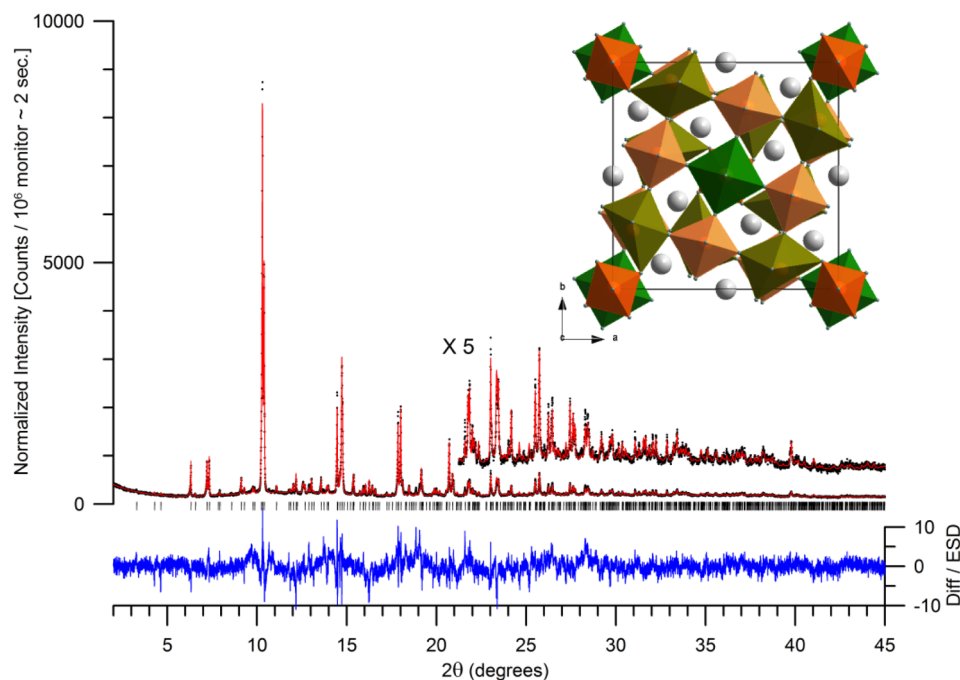


Figure 1. Refinement of the structure of $\text{CsTlCl}_3\text{-t}$ using SPXD. Lattice parameters $a = 17.2489(2)$ Å and $c = 11.1004(2)$ Å. Space group $I4/m$. The inset shows a schematic view of the structure (Tl^+ inside the green octahedra, Tl^{3+} inside the orange octahedra, and Cs^+ atoms are the gray spheres).

activation barrier for direct electron pair transfer is very large. Increased pressure forces the geometric differences between different oxidation states to become smaller, decreasing the activation barrier and changing the electronic properties from an insulating to a metallic state. Although CsAuX_3 phases are structurally similar to BaBiO_3 and share a similar mixed valence of the B cations, the absence of superconductivity in the former phases suggests that charge disproportionation is not the sole consideration for superconductivity.

Recently, Kotliar et al.¹⁴ explained the high-temperature superconductivity in a large family of materials, including $(\text{Ba,K})\text{BiO}_3$, by a correlation-enhanced strong electron–phonon coupling mechanism. This coupling in CsAuCl_3 was found to be weak, accounting for the absence of superconductivity in agreement with experiments. Nevertheless, on the basis of the correlation-enhanced strong electron–phonon coupling mechanism, they predicted that high-temperature superconductivity could be found in the doped CsAuX_3 -like perovskites: CsTlF_3 and CsTlCl_3 .¹⁵ Both of these Tl compounds are expected to be isostructural with BaBiO_3 , share the same valence electron count, and retain essentially the same band structure near the Fermi level. With these similarities, CsTlF_3 and CsTlCl_3 were predicted to be superconducting with hole doping and pressure to reduce the structural distortions. The critical superconducting temperature (T_C) was predicted to be ~ 30 K for CsTlF_3 and ~ 20 K for the Cl analogue, under an optimal hole doping level (~ 0.35 f.u.⁻¹) and moderately high pressures (between ~ 10 and ~ 2 GPa).¹⁵ Recently, similar materials, notably the Rb analogues, have been studied theoretically by Schoop et al.,¹⁶ who contrasted them with BaBiO_3 and predicted the possibility of superconductivity if they were hole doped and compared the stability of possible crystal structures upon charge disproportionation.

Here we report the synthesis and properties of CsTlX_3 ($X = \text{Cl}$ or F) with $\text{Tl}^+/\text{Tl}^{3+}$ charge ordering. To the best of our knowledge, they are the first inorganic perovskites with charge

ordering of Tl cations. A previous synthesis of CsTlCl_3 was described in an unpublished dissertation in 1993.¹⁷ We have characterized both materials, determined their crystallographic structures, and confirmed Tl^{+3+} mixed valence in both compounds. In addition, we have studied the effect of pressure on the properties. We are currently working on optimally doping these phases with the goal of finding superconducting materials.

■ DETAILS OF THE SYNTHESIS

The synthesis of these thallium halides is not trivial because of the toxicity of Tl and the hygroscopic character of the samples. CsTlCl_3 was obtained as fused and intergrown yellow-orange crystals of several millimeters. A precursor of $\text{Cs}_2\text{TlCl}_5 \cdot \text{H}_2\text{O}$ was prepared by dissolving 3 g of CsCl in 10 mL of HCl (37%) and 0.3 g of Tl_2O_3 in 3 mL of HCl (37%). When these solutions were combined, a precipitate appeared (mainly CsCl); after the addition of 100 mL of water, another precipitate, identified as $\text{Cs}_2\text{TlCl}_5 \cdot \text{H}_2\text{O}$,¹⁸ appeared (Figure S1a in section 1 of the Supporting Information). In a second step, $\text{Cs}_2\text{TlCl}_5 \cdot \text{H}_2\text{O}$ and TlCl were mixed and ground inside a glovebox, vacuum-sealed in a silica tube, and heated to 600 °C over 12 h. The synchrotron powder X-ray diffraction (SPXD) pattern of the product (Figure 1) is characteristic of a distorted tetragonal perovskite. Henceforth, this phase will be designated as $\text{CsTlCl}_3\text{-t}$. An alternative method of synthesis with TlCl , CsCl , and $\text{TlCl}_3 \cdot x\text{H}_2\text{O}$ also yielded $\text{CsTlCl}_3\text{-t}$ by PXD (Figure S2a,b in section 1 of the Supporting Information). A different CsTlCl_3 phase is obtained when anhydrous Cs_2TlCl_5 is used as a starting material. [Cs_2TlCl_5 is formed by heating $\text{Cs}_2\text{TlCl}_5 \cdot \text{H}_2\text{O}$ at 150 °C (Figure S1b of the Supporting Information).] Stoichiometric Cs_2TlCl_5 and TlCl are ground in the glovebox, placed in a vacuum-sealed silica tube, and heated to 600 °C over 12 h. The crystals obtained are lighter yellow-orange (inset of Figure 2a) but similar in size and shape to the tetragonal phase. This phase has a structure different from that of the $\text{CsTlCl}_3\text{-t}$ polymorph. It is also perovskite-related, but many tetragonal peaks are absent, being explained with a cubic symmetry and designated as $\text{CsTlCl}_3\text{-c}$ (Figure 2a). Thus, we have observed the existence of two different phases in the CsTlCl_3 system, and a study of both crystal structures is described below. The appearance of different phases seems to be related to the

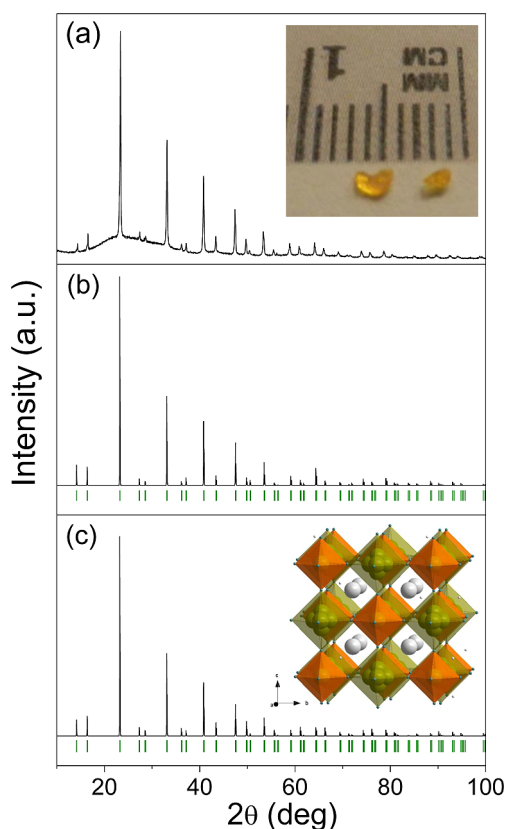


Figure 2. Comparison of (a) experimental PXD of $\text{CsTlCl}_3\text{-c}$. The inset shows crystals of $\text{CsTlCl}_3\text{-c}$. (b) Simulation from SCD using the whole-site anharmonic ADP model. (c) Simulation from SCD using the split atom model. The inset shows a schematic view of the structure with this model. The green spheres represent the disordered Tl^+ atoms and the orange spheres Ti^{3+} in the regular O_h site.

quantity of water in the starting materials; unless they are thoroughly dried, the $\text{CsTlCl}_3\text{-t}$ phase appears. Infrared spectroscopy and thermal

gravimetric analysis confirmed the absence of water or hydroxide in either phase (Figures S3–S5 in section 1 of the Supporting Information).

CsTlF_3 was also prepared in a glovebox to avoid contact of the material with air and moisture. The synthesis is performed in two steps: (i) the preparation of TIOF (source of Ti^{3+}) via addition of Ti_2O_3 to a solution of HF (37%) and (ii) the $\text{CsF} + \frac{1}{2}\text{TlF} + \frac{1}{2}\text{TIOF} + x\text{C}_2\text{F}_4$ ($x = 2\text{--}3$) reaction. Polytetrafluoroethylene (C_2F_4) is required as the source of F. The starting materials were pressed into a pellet, covered with Pt foil (required to avoid the competing reaction with the silica tube producing Cs_2SiF_6), and heated in an evacuated sealed silica tube at 500°C for 12 h. The obtained material was washed in methanol to eliminate TlCl and CsCl impurities. The SPXD pattern is shown in Figure 3. The experimental details of the techniques used for the characterization of the samples are presented in section 1 of the Supporting Information.

RESULTS AND DISCUSSION

We performed chemical analysis by inductively coupled plasma (ICP) mass spectrometry. The composition of $\text{CsTlCl}_3\text{-c}$ (52.62% Cs and 47.38% Tl) and that of $\text{CsTlCl}_3\text{-t}$ (53.64% Cs and 46.36% Tl) are very close to the refined (*vide infra*) Tl vacancy concentration: 55:45 Cs:Tl ratio for $\text{CsTlCl}_3\text{-c}$ (Table 1) and 54:46 Cs:Tl ratio for $\text{CsTlCl}_3\text{-t}$ (Table 5). For the fluoride analogue, it was not possible to obtain a reliable chemical analysis, because of the presence of impurity phases that also contain Cs and/or Tl. However, the synchrotron X-ray diffraction data identified all phases present, with the major ($\sim 77\%$) one being the cubic perovskite phase CsTlF_3 (see below).

Crystal Structures. $\text{CsTlCl}_3\text{-c}$. The crystal structure of CsTlCl_3 phases is complex, and different techniques were required for their solution. To help determine the $\text{CsTlCl}_3\text{-c}$ structure, selected area electron diffraction (SAED) was undertaken. Because the sample decomposed when the electron beam was focused into a high-intensity spot, it was not possible to perform imaging (HRTEM and HR-STEM) and convergent-beam electron diffraction (CBED). The unit cell parameters determined by SAED provided sufficient

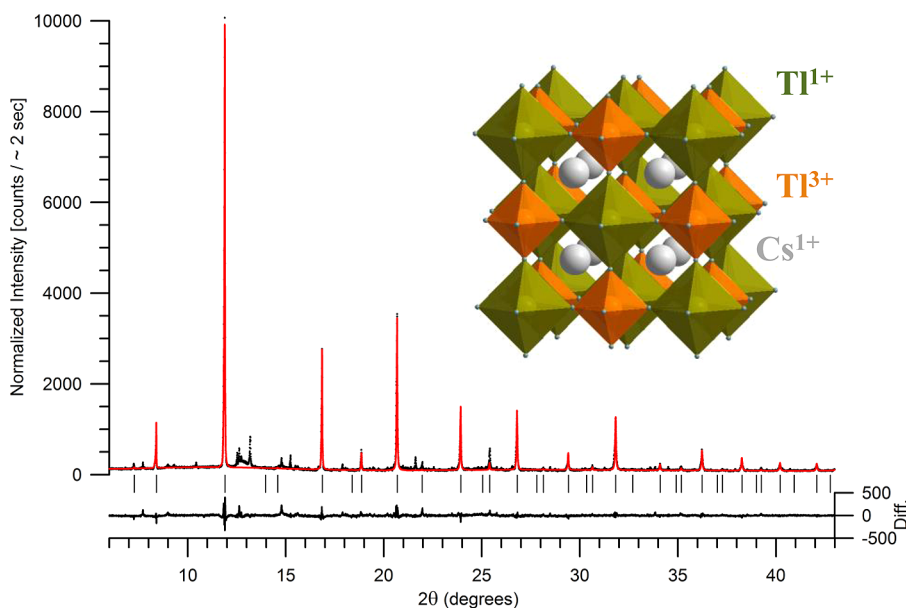
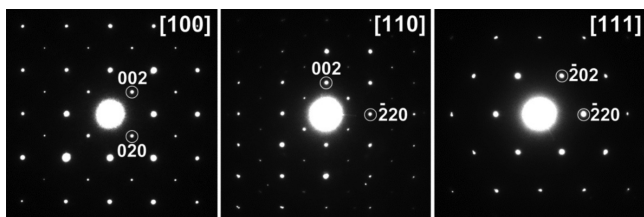


Figure 3. Rietveld refinement of CsTlF_3 in the $Fm\bar{3}m$ space group with $a = 9.5449(1)\text{ \AA}$, using SPXD. Black dots are raw data, and the red line is the computed model of CsTlF_3 ; however, all phases were included in the calculation of the difference curve. The inset shows the cubic double perovskite structure of CsTlF_3 .

Table 1. Atomic Positions, Anharmonic Displacement Parameters, and Site Occupancies for CsTlCl₃-c Refined in the *Fm* $\bar{3}m$ Space Group (No. 225) with Cell Parameter *a* = 10.8226(14) Å

	Cs	Tl1	Tl2	Cl1	Cl2
<i>x</i>	1/4	0	1/2	0.2376(10)	0
<i>y</i>	1/4	0	0	0	0.165(4)
<i>z</i>	1/4	0	0	0	0.165(4)
Occ(fraction)	1.000	1.000	0.68(5)	0.84(4)	0.16(4)
<i>U</i> ₁₁	0.092(11)	0.0245(11)	0.151(7)	0.028(5)	0.03(2)
<i>U</i> ₂₂	0.092(11)		0.151(7)	0.049(4)	0.03(2)
<i>U</i> ₃₃	0.092(11)		0.151(7)	0.049(4)	0.03(2)
<i>U</i> ₁₂	0		0	0	0
<i>U</i> ₁₃	0		0	0	0
<i>U</i> ₂₃	0		0	0	0.01(2)
<i>C</i> ₁₂₃	0.007(7)				
<i>D</i> ₁₁₁₁	−0.007(5)		−0.03(3)		
<i>D</i> ₁₁₂₂	0.000(3)		−0.071(10)		
<i>E</i> ₁₁₁₂₃	−0.0004(7)				
<i>F</i> ₁₁₁₁₁₁	−0.004(2)		−0.08(2)		
<i>F</i> ₁₁₁₁₂₂	−0.0002(4)		−0.013(2)		
<i>F</i> ₁₁₂₂₃₃	0.0004(4)		0.011(4)		

evidence to select the proper space group, *Fm* $\bar{3}m$. All SAED patterns could be indexed with the cell parameters (*a* = 10.84 Å) determined from the PXD data and space group *Fm* $\bar{3}m$ (Figure 4). The refinement of the CsTlCl₃-c structure was

**Figure 4.** Representative selected area electron diffraction patterns of CsTlCl₃-c, indexed in the F-centered cell described in the text.

conducted with single-crystal X-ray diffraction (SCD) data collected at 100 K. The structural refinement was performed with JANA2006.¹⁹ The initial SCD model was based on the known cubic double perovskite, *Fm* $\bar{3}m$, structure with atoms in these positions: Cs⁺ at A (1/4 1/4 1/4), Tl³⁺(Tl1) at B (0 0 0), Tl⁺(Tl2) at B' (1/2 0 0), and Cl[−](Cl1) anions at (*x* 0 0) with *x* ~ 0.239(1). The occupancy of the Cl[−] anion in this site was found to be deficient by ~16%, and a second Cl site (Cl2) with an approximate occupancy of 16% was found 1.9 Å away, at (0 0.165(4) 0.165(4)). Large residuals in the difference electron density maps in the vicinity of Tl2 (1/2 0 0) and Cs (1/4 1/4 1/4) indicated significant disorder around these two positions. We explained the residuals using Gram–Charlier anharmonic displacement parameters up to six orders. The crystallographic details of this refinement are presented in Table S1 of the Supporting Information, the final atomic parameters in Table 1, and the average bond distances in Table 2. The PXD pattern calculated from this refinement (Figure 2b) is very similar to the experimental PXD data (Figure 2a). The occupancy of Tl2 in the B' site was found to be less than full, namely 0.68(5), with the highly correlated intensity weighting scheme based upon a *p* of 0.10 for [$\sigma(I) + p \times I^4$] in JANA2006. Thus, the B' site appears to contain some vacancies and requires the presence of both Tl⁺ and Tl³⁺ in this position for charge balance but is mainly occupied by Tl⁺. This result would explain

Table 2. Bond Lengths (angstroms) for CsTlCl₃-c from Refinement in JANA2006 Using Anharmonic Displacement Parameters^a

Cs–Cl1	12 × 3.828(1)
Cs–Cl2	12 × 2.97(2)
Tl1–Cl1	6 × 2.58(1)
Tl1–Cl2	6 × 2.59(5)
Tl1–Cl2	6 × 2.59(5)
Tl2–Cl1	6 × 2.83(1)

^aThe values of the distances for the cation positions, Cs and Tl2, are average values with maximal displacements from their site centers of 0.5 and 0.9 Å, respectively (see the text).

the shorter Tl2–Cl1 distances found [2.83(1) Å] compared with the expected bond distance of 3.31 Å from the Tl⁺–Cl Shannon sum of radii,²⁰ while Tl1–Cl distances match very well with six-coordinate Tl³⁺ cations (2.70 Å). Vacancies in other perovskite-like chlorides (Cs₂MCl₆ with K₂PtCl₆ structural type, *Fm* $\bar{3}m$) have been reported and take place when M is a tetravalent cation, such as Sn, Ta, Re, W, etc.;^{21–24} 12-coordinated Cs⁺ is primarily bonded to Cl1 (refined occupancy of 0.84 for Cl1) at distances of 3.828(1) Å, which agrees well with the Shannon sum of radii (3.69 Å). There are many fewer (~0.16 of the time) Cs–Cl2 bonds with shorter distances [2.97(2) Å], which are probably due to some Tl⁺ at this position or vacancies, consistent with the refined stoichiometry. We also investigated the possible existence of oxygen over either Cl[−] site; however, O^{2−} did not refine as well as Cl[−] and gave unrealistic metal–oxide bond lengths. Further examination of the two Cl[−] sites reveals that only Cl1 atoms are close enough to Tl2 to form bonds with it, but both Cl1 and Cl2 form bonds (but not at the same time) with Cs and Tl1 (Table 2). The appearance of an interstitial anion (as Cl2 in our case) has been observed in some oxygen-containing double perovskites with large B-site cations (as Tl⁺ in our case), such as Sr₂(Sr_{1−*x*}M_{1+*x*})O₆ (M = Nb or Ta) and Sr₂MSbO₆ (M = Ca, Sr, or Ba).^{25–27} The large B-site cation causes nonharmonic atomic displacements that drive some oxygens to the interstitial site and leave oxygen vacancies in the original positions.

Table 3. Atomic Coordinates, Occupancies, and Displacement Parameters (square angstroms) for CsTlCl₃-c, with the Split Atom Model^a

	Cs1	Cs2	Cs3	Tl1	Tl2A	Tl2B	Tl2C	Cl1	Cl2
<i>x</i>	1/4	0.2791(10)	1/4	0	1/2	0.4180(3)	0.4414(12)	0.2373(2)	0
<i>y</i>	1/4	0.2209(10)	1/4	0	0	0	0	0	0.1682(8)
<i>z</i>	1/4	0.2209(10)	0.2059(12)	0	0	0	-0.586(12)	0	0.1682(8)
Occ(fraction)	0.30(1)	0.30(2)	0.40(3)	1.000	0.026(2)	0.62(1)	0.13(1)	0.82(3)	0.18(3)
<i>U</i> (eq)	0.038(1)	0.038(1)	0.038(1)	0.024(1)	0.024(1)	0.024(1)	0.024(1)	0.042(1)	0.034(3)
<i>U</i> ₁₁					0.038(2)	0.038(2)	0.038(2)	0.028(1)	0.033(5)
<i>U</i> ₂₂					0.017(1)	0.017(1)	0.017(1)	0.048(1)	0.034(4)
<i>U</i> ₃₃					0.017(1)	0.017(1)	0.017(1)	0.048(1)	0.034(4)
<i>U</i> ₁₂					0.02(8)	0.02(8)	0.01(10)	0	0
<i>U</i> ₁₃					-0.01(6)	-0.01(6)	-0.03(5)	0	0
<i>U</i> ₂₃					0.013(3)	0.013(3)	0.03(10)	0	-0.013(5)

^aThe isotropic displacement parameters, *U*(eq), are defined as one-third of the trace of the orthogonalized *U*^{ij} tensor. The anisotropic displacement factor exponent takes the form $-2\pi^2(h^2a^{*2}U^{11} + \dots + 2hka^*b^*U^{12})$.

Another model with split positions for the atoms (low symmetry disorder of the cations about their high-symmetry sites) in SHELXL²⁸ was also used to explain the nonspherical electron density and better quantify the apparently anharmonic displacements of Cs and Tl atoms about sites A and B', respectively. Partially weighted Cs atoms were placed at the A site and also at two unique sites nearby, yielding, after application of the site symmetry, a regular polygon with 10 vertices of partially weighted Cs atoms around the central Cs atom at (1/4 1/4 1/4) with average distances from (1/4 1/4 1/4) of approximately 0.5 Å. A similar procedure for Tl2 in the B' site yielded a regular polygon with 18 vertices of Tl atoms spaced ~0.9 Å from the central Tl at (1/2 0 0). In this model, the occupancy sum of all partially weighted Tl2 atoms in the B' site was found to be less than full. The crystallographic details of the split atom refinement are shown in Table S2 of the Supporting Information. The atomic and anisotropic displacement parameters are listed in Table 3 and the bond distances in Table 4. The PXD pattern calculated from this split atom

distances in the range of 3.41–3.87 Å are comparable to the Shannon sum of 3.69 Å for 12-coordinate Cs, while for 0.16 of the time, shorter Cs–Cl2 bonds are found for Cs1, Cs2, and Cs3 with Cs–Cl bond lengths in the range of 2.56–3.46 Å and a coordination number of 6; both observations are consistent with the presence of Tl⁺ or vacancies at these Cs positions. The Tl1–Cl1 and Tl1–Cl2 distances are all 2.57 Å for the six-coordinate Tl and agree well with the expected (Shannon) Tl³⁺–Cl distance of 2.69 Å. The triply disordered Tl2 distances appear to be approximately six-, four-, or two-coordinate for Tl2A (six Tl2A–Cl1 distances are 2.84 Å), Tl2B (four Tl2B–Cl1 distances are 2.98 Å, and the one 1.96 Å distance is ignored as a vacancy of Tl2B), or Tl2C (two Tl2C–Cl1 distances are 2.98 Å, and the two 2.30 Å distances are ignored as vacancies of Tl2C), respectively. As in the anharmonic displacement model, these distances are only to Cl1 and not Cl2 and are always shorter than the expected (Shannon) 3.31 Å Tl³⁺–Cl distance and most likely can be explained by the presence of some Tl³⁺ or vacancies. For comparison, the main Cs⁺–Cl (~3.82 Å) and Tl³⁺–Cl (~2.58 Å) distances obtained in both models are comparable with those in similar compounds, including Cs₂TlCl₅ (Cs–Cl distance of 3.6816 Å and Tl³⁺–Cl distance of 2.5963 Å)³¹ and Tl₂Cl₃ (Tl³⁺–Cl distance of ~2.57 Å).³² Tl⁺–Cl distances are difficult to compare with those of other compounds because there are likely to be some vacancies, as well as some Tl³⁺ in those positions; moreover, Tl⁺ at the relatively low (i.e., ≤6) coordination is rare.

CsTlCl₃-t. Several tilt series of SAED data were taken from different crystallites to determine the unit cell. The compound showed clear superstructure reflections, as was evidenced from the two most prominent zones shown in Figure 5. To index all the reflections, a supercell was needed, with the following cell parameters: *a* ≈ *b* ≈ 17.0 Å, and *c* ≈ 11.0 Å. The relationship

Table 4. Bond Lengths (angstroms) for CsTlCl₃-c, Using the Split Atom Model

Cs1–Cl1	12 × 3.8288(5)
Cs1–Cl2	1 × 2.981(5)
Cs1–Cl2	6 × 2.981(5)
Cs2–Cl1	6 × 3.856(2), 3 × 3.412(14)
Cs2–Cl2	3 × 2.735(9), 3 × 3.126(7)
Cs2–Cl2	3 × 2.735(9), 3 × 3.464(18)
Cs3–Cl1	4 × 3.508(9), 2 × 3.8415(13), 2 × 3.875(2)
Cs3–Cl2	2 × 2.555(13), 4 × 3.156(9)
Cs3–Cl2	2 × 3.421(13), 4 × 2.876(4)
Tl1–Cl1	6 × 2.569(2)
Tl1–Cl2	6 × 2.575(13)
Tl1–Cl2	6 × 2.575(13)
Tl2A–Cl1	6 × 2.843(2)
Tl2B–Cl1	4 × 2.978(2), 1 × 1.955(4)
Tl2C–Cl1	2 × 2.297(9), 2 × 2.981(6)

refinement is illustrated in Figure 2c, together with a schematic view of the proposed structure. This type of refinement has been previously reported in other, similarly disordered systems, such as Ni_{1+δ}Sn or LaNi₅.^{29,30} The obtained distances with this model are similar to that of the Gram–Charlier anharmonic displacement model. The Cs1–Cl1, Cs2–Cl1, and Cs3–Cl1

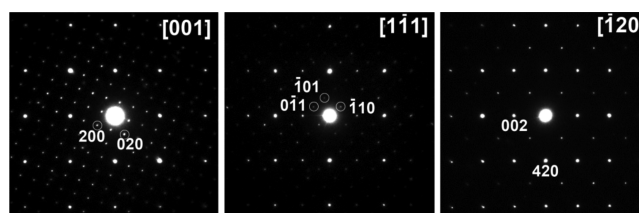
**Figure 5. Three most prominent zones from the series taken from CsTlCl₃-t. Patterns are indexed in the supercell mentioned in the text.**

Table 5. Unit Cell, Positional, and Displacement Parameters and Site Occupancies for CsTlCl₃-t Refined from SXPd in the I4/m Space Group (No. 87), with Cell Parameters $a = 17.2489(2)$ Å and $c = 11.1004(2)$ Å^a

atom	Wyckoff	x	y	z	Occ(fraction)	U _{iso}
Cs1	4d	0	0.5	0.25	1	0.07(1)
Cs2	16i	0.2138(3)	0.1117(2)	0.2750(4)	1	0.07(1)
Tl1	2a	0	0	0	1	0.032(1)
Tl2	2b	0	0	0.5	0.61(1)	0.032(1)
Tl3	8h	0.0942(3)	0.3023(2)	0.5	1	0.0315(6)
Tl4	8h	0.0840(3)	0.2568(2)	0	0.82(1)	0.031(6)
Cl1	4e	0	0	0.231(3)	1	0.071(2)
Cl2	16i	0.087(1)	0.295(1)	0.265(1)	1.000	0.071(2)
Cl3	8h	0.122(1)	0.073(2)	0	1	0.071(2)
Cl4	8h	0.135(2)	0.453(3)	0.5	1	0.071(2)
Cl5	8h	0.253(2)	0.259(2)	0.5	1	0.071(2)
Cl6	8h	-0.059(1)	0.339(2)	0.5	1	0.071(2)
Cl7	8h	0.048(2)	0.172(2)	0.5	1	0.071(2)

^aAgreement factors: $R_p = 5.15\%$, $R_{exp} = 3.51\%$, $R_{wp} = 6.61\%$, $R_{bragg} = 3.1\%$, and $\chi^2 = 3.54$.

between this supercell and the cell of a simple tetragonal double perovskite with subcell $a \approx b \approx 7.7$ Å and $c \approx 11.0$ Å is given by the transformation matrix

$$\mathbf{P} = \begin{bmatrix} 1 & -2 & 0 \\ 2 & 1 & 0 \\ 0 & 0 & 1 \end{bmatrix}$$

which yields a 5-fold increase in the unit cell volume and a resultant tetragonal superlattice of $5^{1/2}\mathbf{a} \ 5^{1/2}\mathbf{b} \ \mathbf{c}$. From the analysis of the reflection conditions and intensity distributions in the ED and SPXD patterns, combined with prediction of the probable space group by SPUDS,³³ space group $I4/m$ was derived. An initial model for the structure was obtained from precision electron diffraction data (PED). The details of the PED experiment and the structure solution from the PED data can be found in section 3 of the Supporting Information. The model was ultimately refined with SPXD. In this structure, there are two positions for Cs, four for Tl (being Tl1 and Tl3 with mainly Tl³⁺ and Tl2 and Tl4 with Tl⁺), and seven for Cl. Sites Tl2 and Tl4 have an occupancy significantly less than unity. A schematic view of the structure together with the refinement of the structure with SPXD is illustrated in Figure 1. The atomic positions are listed in Table 5 and the bond distances in Table 6. The structure is basically formed by

corner-sharing TlCl₆ octahedra (O_h) with Cs in the voids. Some of the TlCl₆ O_h octahedra are highly distorted, producing a strong tilting of other O_h octahedra. The reason for these distortions could be related to the lone pair effect of the Tl⁺ cation together with its large size. For example, Tl4Cl₆ species are highly distorted from ideal O_h species, producing a tilting of Tl1Cl₆ of $\sim 45^\circ$ relative to the orientation of Tl2Cl₆ and Tl3Cl₆ (inset of Figure 1). The Tl1–Cl and Tl3–Cl bond distances are consistent with what is expected for the Tl³⁺–Cl distance. The Tl2–Cl and Tl4–Cl distances are consistent with, but slightly shorter than, what is expected for the Tl⁺–Cl distance; this finding is likely due to the presence of some vacancies and/or some Tl³⁺ over the Tl2 and Tl4 positions. For this set of Tl sites, which are either Tl³⁺ (Tl1 and Tl3) or mostly Tl⁺ (Tl2 and Tl4), we confirm that there is charge ordering in the structure. It is also worth noting that the dramatic superlattice of $5^{1/2}\mathbf{a} \ 5^{1/2}\mathbf{b} \ \mathbf{c}$ determined for this phase is reported for the first time in a perovskite-related material.

CsTlF₃. The crystallographic structure was refined from SPXD data in the $Fm\bar{3}m$ space group ($R_{wp} = 9.8\%$). The refined cell parameter was $a = 9.5449(1)$ Å. The position of F was (0.277(1), 0, 0). The observed Tl³⁺–F and Tl⁺–F distances were 2.12(1) and 2.65(1) Å, respectively, consistent with Tl³⁺–F and Tl⁺–F distances in other phases, including Tl³⁺ in Cs₃TlF₆ (2.02 Å)³⁴ and Tl⁺ in TlF (2.4–2.7 Å).³⁵ The Tl–F distances are also comparable with those expected from the ionic radius sums of 2.21 Å for Tl³⁺–F distances and 2.83 Å for Tl⁺–F distances.²⁰ Figure 3 shows the refinement of the structure in the $Fm\bar{3}m$ cubic model with the presence of the impurities: Cs₃TlF₆ ($I4/mmm$), 14 wt %; Tl₂O₃ ($Ia\bar{3}$), 6%; CsO₂ ($I4/mmm$), 2%; and TlF ($Pm2a$), 1%. The schematic view of the structure of CsTlF₃ is shown in the inset of Figure 3. The discovery of cubic structures in CsTlX₃ is a good starting point in search of superconductivity because, in theory, superconductivity in these phases could only be achieved in cubic perovskites.¹⁵

X-ray Absorption Spectroscopy (XAS). We performed XAS to verify the Tl^{1+/3+} mixed-valence character of thallium; Tl³⁺ involves two 6s-orbital holes. The Tl–L₃ edge XAS signature of the Tl⁺ to Tl³⁺ change is a chemical shift of the main edge to a higher energy and the appearance of a shoulder pre-edge feature caused by transitions into the empty 6s hole states.³⁶ These same signatures are well-known at the Bi–L₃ edge to evidence the Bi³⁺ to Bi⁵⁺ change.^{37–39} In Figure 6a, the

Table 6. Bond Lengths (angstroms) for CsTlCl₃-t

Tl1–Cl3	4 × 2.45(3)
Tl1–Cl1	2 × 2.56(3)
Tl2–Cl1	2 × 2.99(3)
Tl2–Cl7	4 × 3.07(3)
Tl3–Cl7	2.39(3)
Tl3–Cl2	2 × 2.62(1)
Tl3–Cl4	2.64(3)
Tl3–Cl6	2.71(3)
Tl3–Cl5	2.84(3)
Tl4–Cl5	2.82(3)
Tl4–Cl4	2.93(3)
Tl4–Cl2	2 × 3.01(1)
Tl4–Cl3	3.26(3)
Tl4–Cl6	3.45(3)
minimal Tl–Cs	4.53(1)
minimal Cl–Cs	3.44(1)

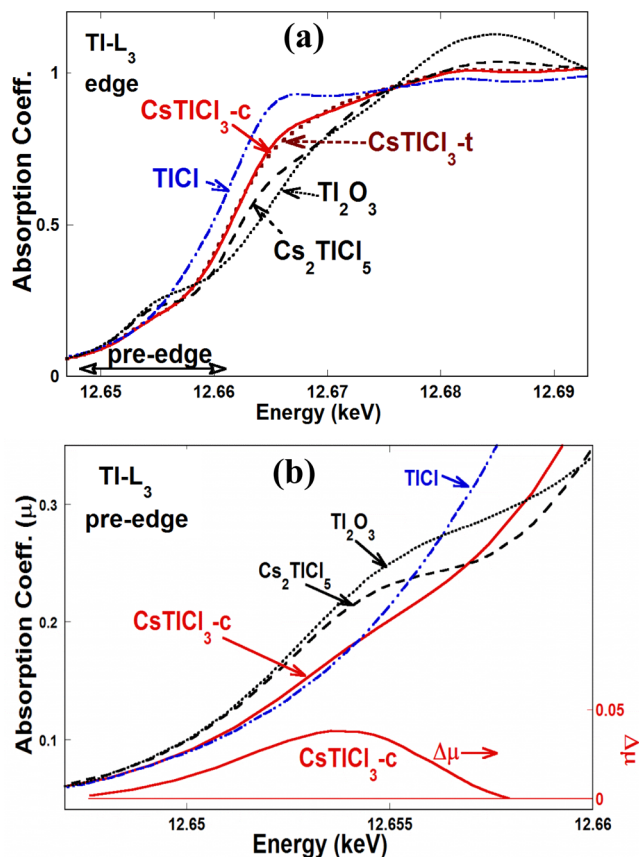


Figure 6. (a) TI-L₃ edges of CsTlCl₃-t, CsTlCl₃-c, and Ti₂O₃, Cs₂TlCl₅, and TlCl standards. (b) Expanded view of the TI-L₃ pre-edges. The 6s hole-related feature of CsTlCl₃-c (extracted by subtraction of an sp line fit background) is also shown on an enlarged vertical scale at the bottom.

TI-L₃ edge spectra of CsTlCl₃-t and CsTlCl₃-c are compared to those of TI⁺ and TI³⁺ standards. Assigning the nominal chemical shift as the energy at which the normalized absorption coefficient value first rises to the $\mu = 0.5$ value, we find the chemical shifts of CsTlCl₃ phases are clearly intermediate between those of TI⁺ and TI³⁺ standards, supporting their averaged valence. The disparity between the energies of the $\mu = 0.5$ chemical shift points of the TI³⁺ standards, Cs₂TlCl₅ and Ti₂O₃, underscores the qualitative nature of the inference of the intermediate valence of both CsTlCl₃ phases. In Figure 6b, the pre-edge regions of the spectra are plotted on an expanded scale with the CsTlCl₃-t spectrum being left out because it is essentially identical to that of CsTlCl₃-c. The first point to note is that the TI⁺Cl spectrum exhibits a monotonic concave upward curvature over the entire pre-edge region, consistent with the absence of any 6s hole states (6s²). In contrast, the TI³⁺ standards manifest pronounced pre-edge shoulder features consistent with the presence of two 6s orbital holes (6s⁰). CsTlCl₃-c shows a clear, albeit not dramatic, shoulder feature supporting the presence of 6s hole states and a TI⁺/TI³⁺ valence state. To emphasize the presence of the shoulder, an sp line fit to the data above and below this feature has been subtracted, to obtain an estimate of just the shoulder feature portion ($\Delta\mu$), shown in the bottom of Figure 6b. The TI-L₃ edge of CsTlF₃ and the Cl-K edge of CsTlCl₃ phases are presented in section 4 of the Supporting Information.

Raman Spectroscopy. We have studied the effect of pressure on the Raman spectra of CsTlCl₃ phases (Figure 7) to

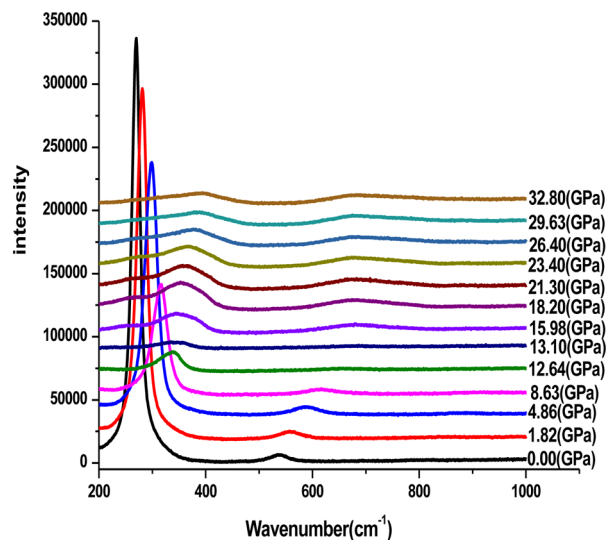


Figure 7. Pressure dependence of the Raman spectra of CsTlCl₃-c at room temperature.

investigate a possible transition to a single valence state (TI⁺/TI³⁺ to TI²⁺). Further, we conducted frozen phonon calculations with hybrid density functional theory (DFT) for the TI-Cl stretching mode of cubic CsTlCl₃, and the calculated phonon frequency was found to be 277 cm⁻¹, in excellent agreement with that observed at 270 cm⁻¹ (Figure 7). With increasing pressure, the 270 cm⁻¹ Raman TI-Cl mode moves to a higher frequency (as expected due to the compression of the bonds) but does not completely disappear, as is the case for CsAuX₃, where Au⁺³⁺ charge ordering is suppressed at a critical pressure.⁴⁰ This result does not rule out the possibility of the compound becoming superconducting with optimal doping, because a similar effect was observed in undoped BaBiO₃, where a single valence state by merely applying high pressure, without doping, could not be achieved.⁴¹ The pressure-dependent Raman spectra of CsTlCl₃-t indicate similar behavior.

Resistivity Measurements under Pressure. We measured the resistance of CsTlCl₃-c at high pressures to study a possible transition to a metallic state. The resistance is too high to be measurable below 50 GPa. Figure 8 shows the resistance versus temperature at 53, 58, and 60 GPa; CsTlCl₃-c becomes more conductive, with a change from transparent to opaque with an increasing pressure that indicates the narrowing of the band gap. The activation energy (E_g), which is proportional to the energy gap and can be calculated from the relation $\ln R \sim E_g/(2k_B T)$, was found to be 0.245, 0.233, and 0.212 eV for 53, 58, and 60 GPa, respectively. These values are 1 order of magnitude smaller than the optical band gap predicted theoretically [2.1 eV (Figure 9)] and measured experimentally [2.5 eV (inset of Figure 9)] for CsTlCl₃-c without pressure. These results indicate that the band gap decreases with pressure, in good agreement with theory. The magnetic behavior of the materials reflects essentially insulating/diamagnetic properties as discussed in section 5 of the Supporting Information.

First-Principles Calculations. One of the important characteristics of the compounds is that the semilocal local

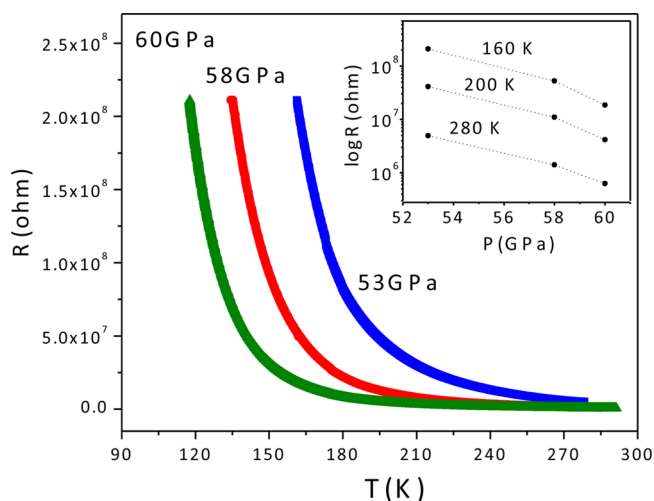


Figure 8. Resistance vs temperature of $\text{CsTiCl}_3\text{-c}$ measured under applied pressures of 53, 58, and 60 GPa (measuring current I of 0.1 μA). The inset shows resistance vs pressure at several fixed temperatures.

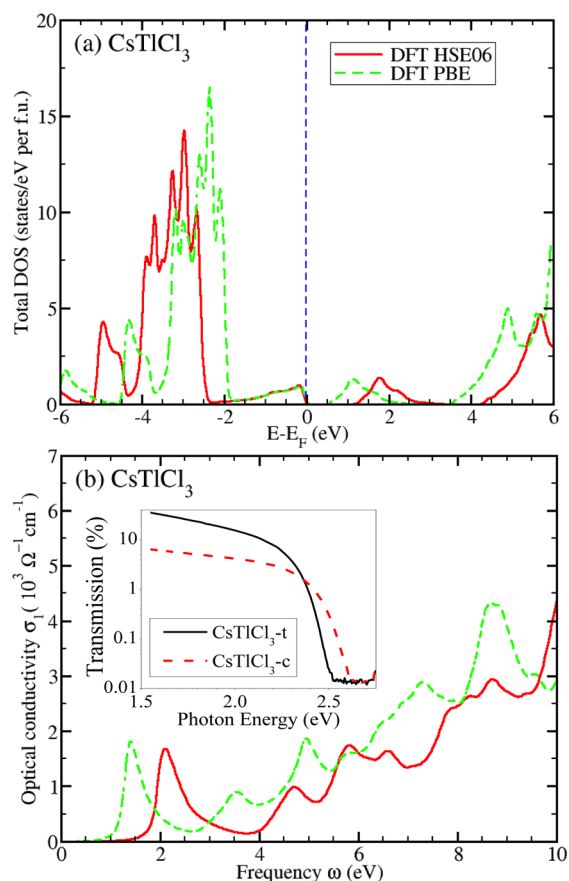


Figure 9. (a) Total density of states (DOS). (b) Calculated optical conductivity of $\text{CsTiCl}_3\text{-c}$. The inset shows the measured optical conductivity of $\text{CsTiCl}_3\text{-c}$ and $\text{CsTiCl}_3\text{-t}$.

density approximation (LDA) and generalized gradient approximation (GGA) within the DFT framework substantially underestimate the structural distortions and band gaps, and incorporating nonlocal correlations (long-range exchange) with HSE-like (screened) hybrid functional brings both quantities to much better agreement with experiments.^{14,15} To test this, we

conducted first-principles DFT calculations with the VASP code⁴² for $\text{CsTiCl}_3\text{-c}$ and compared the results with those of available experiments. In addition to a generalized gradient approximation (PBE version)⁴³ exchange-correlation functional, a screened hybrid functional HSE06⁴⁴ has been adopted to account for the nonlocal correlation/long-range exchange in this compound. Using the experimental lattice constant $a = 10.8226(14)$ Å for $\text{CsTiCl}_3\text{-c}$, we relax the structure within the $Fm\bar{3}m$ space group. The relaxed Cl position (x 0 0) is $x = 0.2392$ from DFT-PBE and $x = 0.2359$ from DFT-HSE06. In comparison with the experimental value of $x = 0.2376(10)$, DFT-PBE underestimates the Cl breathing distortion while DFT-HSE06 slightly overestimates it, similar to the case for BaBiO_3 . Likewise, the DFT-HSE06 optimized value $x = 0.226$ of the F position (x 0 0) in CsTiF_3 at ambient pressure agrees better with the experimental value $x = 0.223(1)$ [equivalent to 0.277(1) in a different setting] than the DFT-PBE optimized value $x = 0.230$ (see section 6 of the Supporting Information). Adopting the experimental crystal structure, we compute the total density of states (DOS) and optical conductivity of $\text{CsTiCl}_3\text{-c}$ (panels a and b of Figure 9, respectively): $\text{CsTiCl}_3\text{-c}$ is an insulator with a (indirect) band gap of ~ 1.3 eV (0.6 eV) and an optical gap of ~ 2.1 eV (1.4 eV), as computed by DFT-HSE06 (DFT-PBE). The calculated band gap determined by DFT-GGA is much smaller than the DFT-HSE06 value, illustrating the delocalization error of the semilocal nature of the LDA/GGA functional. This delocalization error also has an impact on the positions of the Cl p states and, consequently, the peak positions in optical conductivity. As shown in Figure 9a, the valence bands near the Fermi level are dominated by Cl p states, peaking at approximately -3.0 (-2.4) eV in DFT-HSE06 (DFT-GGA). Correspondingly, the first peak position in the optical conductivity is at ~ 2.1 (1.4) eV (Figure 9b). The DFT-HSE06 optical gap agrees reasonably well with the experimental optical gap of ~ 2.5 eV estimated from the optical experiments in transmission mode (inset of Figure 9b) and is much larger than the result of the corresponding DFT-GGA calculation using the same crystal structure. These results confirm that $\text{CsTiCl}_3\text{-c}$ behaves like BaBiO_3 and could be another member of the family of the “other high-temperature superconductors”.¹⁴

CONCLUSIONS

In conclusion, we have synthesized $\text{Ti}^+/\text{Ti}^{3+}$ mixed-valent CsTiX_3 ($X = \text{F}$ or Cl) materials, which were theoretically predicted to become superconducting with appropriate doping and under pressure. This is the first published report of an inorganic perovskite with $\text{Ti}^+/\text{Ti}^{3+}$ charge ordering stabilized. CsTiCl_3 intergrown transparent yellow-orange crystals were obtained as two phases: a distorted tetragonal ($I4/m$) and a cubic ($Fm\bar{3}m$) phase with interstitial Cl^- balancing Cl^- site vacancies and some Ti^+ vacancies. CsTiF_3 is obtained as a brown polycrystalline material with cubic symmetry ($Fm\bar{3}m$). XAS and Raman spectroscopy unambiguously confirm the presence of $\text{Ti}^+/\text{Ti}^{3+}$. Raman spectra demonstrate that the charge ordering is present even at high pressures. The resistance of the cubic CsTiCl_3 is too high to measure under ambient conditions, but it decreases when high pressures are applied. First-principles calculations of the crystal structure, density of states, and optical conductivity, together with the corresponding experimentally determined properties of cubic CsTiCl_3 , indicate that it is similar to BaBiO_3 , and a potential superconductor, when it is optimally doped.

■ ASSOCIATED CONTENT

■ Supporting Information

Details of PXD of the precursors and different obtained materials, TGA and DSC analysis, IR spectroscopy, experimental details, crystallographic details of the two models used to explain the cubic CsTlCl₃-c phase, details of the structure solution from PED data, including the initial model, XAS Tl-K edge of CsTlF₃ and Cl-K edge of CsTlCl₃ phases, magnetic measurements, and DOS and optical conductivity of CsTlF₃. This material is available free of charge via the Internet at <http://pubs.acs.org>.

■ AUTHOR INFORMATION

Corresponding Author

*E-mail: martha@rutchem.rutgers.edu.

Notes

The authors declare no competing financial interest.

■ ACKNOWLEDGMENTS

This work was supported by National Science Foundation Grant DMR-0966829, U.S. Department of Defense Grant VV911NF-12-1-0172, and Rutgers University (BOG) grants. Z.P.Y. and G.K. were supported by the AFOSR-MURI program for better and higher temperature superconductors. Use of the National Synchrotron Light Source, Brookhaven National Laboratory, was supported by the U.S. Department of Energy, Office of Science, Office of Basic Energy Sciences, under Contract DE-AC02-98CH10886. We thank Dr. Hongbing Sun and James Elliott for their help with the ICP and IR measurements.

■ REFERENCES

- (1) Müller, K. A.; Bednorz, J. G. *Science* **1987**, *237*, 1133–1139.
- (2) Takagi, H. S.; Uchida, S.; Kitazawa, K.; Tanaka, S. *Jpn. J. Appl. Phys.* **1987**, *26*, L123.
- (3) Sleight, A. W.; Gillson, J. L.; Bierstadt, P. E. *Solid State Commun.* **1975**, *17*, 27–28.
- (4) Cava, R. J.; Batlogg, B.; Krajewski, J. J.; Farrow, R.; Rupp, L. W., Jr.; White, A. E.; Short, K.; Peck, W. F.; Kometani, T. *Nature* **1988**, *332*, 814–816.
- (5) Khan, Y.; Nahm, K.; Rosenberg, M.; Willner, H. *Phys. Status Solidi A* **1977**, *39*, 79–88.
- (6) Cox, D. E.; Sleight, A. W. *Solid State Commun.* **1976**, *19*, 969–973.
- (7) Pei, S.; Jorgensen, J. D.; Dabrowski, B.; Hinks, D. G.; Richards, D. R.; Mitchell, A. W.; Newsam, J. M.; Sinha, S. K.; Vaknin, D.; Jacobson, A. J. *Phys. Rev. B* **1990**, *41*, 4126–4141.
- (8) Elliot, N.; Pauling, L. *J. Am. Chem. Soc.* **1938**, *60*, 1846–1851.
- (9) Tindemans, J. C. M.; Eijndhoven, V.; Verschoor, G. C. *Mater. Res. Bull.* **1974**, *9*, 1667–1670.
- (10) Keller, R.; Fenner, J.; Holtzapfel, W. B. *Mater. Res. Bull.* **1974**, *9*, 1363–1369.
- (11) Kojima, N.; Hasegawa, M.; Kitagawa, H.; Kikegawa, T.; Shimomura, O. *J. Am. Chem. Soc.* **1994**, *116* (25), 11368–11374.
- (12) Matsushita, N.; Ahsbans, H.; Hafner, S. S.; Kojima, N. *J. Solid State Chem.* **2007**, *180*, 1353–1364.
- (13) Wang, S.; Hirai, S.; Shapiro, M. C.; Riggs, S. C.; Geballe, T. H.; Mao, W. L.; Fisher, I. R. *Phys. Rev. B* **2013**, *87*, 054104.
- (14) Yin, Z. P.; Kutepov, A.; Kotliar, G. *Phys. Rev. X* **2013**, *3*, 021011.
- (15) Yin, Z. P.; Kotliar, G. *EPL* **2013**, *101*, 27002.
- (16) Schoop, L. M.; Muehler, L.; Felser, C.; Cava, R. J. *Inorg. Chem.* **2013**, *52*, 5479–5483.
- (17) Richter, R. Thermische, spektroskopische und röntgenographische Untersuchungen von Chlorothallaten(III) der Alkalimetalle. Ph.D. Dissertation, University of Freiburg, Freiburg, Germany, 1993.
- (18) Pratt, J. H. *Am. J. Sci.* **1895**, *49*, 397.
- (19) Petricek, V.; Dusek, M.; Palatinus, L. Jana2006. *The crystallographic computing system*; Institute of Physics: Praha, Czech Republic, 2006.
- (20) Shannon, R. D. *Acta Crystallogr.* **1976**, *A32*, 751–767.
- (21) Brill, T. B.; Gearhart, R. C.; Welsh, W. A. *J. Magn. Reson.* **1974**, *13*, 27–37.
- (22) Yun, H.; Jang, G.-J. *Acta Crystallogr.* **2007**, *E63*, i22–i23.
- (23) Sperka, G.; Mautner, F. A. *Cryst. Res. Technol.* **1988**, *23*, k109–k111.
- (24) Wang, P.; Xu, W.; Zheng, Y.-Q. *Z. Kristallogr. - New Cryst. Struct.* **2003**, *218*, 25.
- (25) Deniard, P.; Caldes, M. T.; Zou, X. D.; Diot, N.; Marchand, R.; Brec, R. *Int. J. Inorg. Mater.* **2001**, *3*, 1121–1123.
- (26) Li, M.-R.; Hong, S.-T. *Chem. Mater.* **2008**, *20* (8), 2736–2741.
- (27) King, G.; Thomas, K. J.; Llobet, A. *Inorg. Chem.* **2012**, *51*, 13060–13068.
- (28) Sheldrick, G. M. *SHELXL97, Program for Crystal Structure Refinement*; University of Göttingen: Göttingen, Germany, 1997.
- (29) Joubert, J.-M.; Cerny, R.; Latroche, M.; Leroy, E.; Guenee, L.; Percheron-Guegan, A.; Yvon, K. *J. Solid State Chem.* **2002**, *166*, 1.
- (30) Leineweber, A.; Oeckler, O.; Zachwieja, U. *J. Solid State Chem.* **2004**, *177*, 936–945.
- (31) Thiele, G.; Richter, R. *Z. Kristallogr.* **1993**, *205*, 131–132.
- (32) Boehme, R.; Rath, J.; Grunwald, B.; Thiele, G. *Z. Naturforsch.* **1980**, *35*, 1366–1372.
- (33) Lufaso, M. W.; Woodward, P. M. *Acta Crystallogr.* **2001**, *B57*, 725–738.
- (34) Bode, V. H.; Voss, E. *Z. Anorg. Allg. Chem.* **1957**, *290*, 1–16.
- (35) Berastegui, P.; Hull, S. *J. Solid State Chem.* **2000**, *150*, 266–275.
- (36) Huan, G.; Greaney, M.; Greenblatt, M.; Liang, G.; Croft, M. *Solid State Ionics* **1988**, *32*, 134–140.
- (37) Li, S.; Greenblatt, M.; Jeon, Y.; Chen, J.; Croft, M. *Physica C* **1991**, *173*, 239–244.
- (38) Yang, T.; Abakumov, A.; Hadermann, J.; Van Tendeloo, G.; Nowik, I.; Stephens, P.; Hemberger, J.; Tsirlin, A.; Ramanujachary, K.; Lofland, S.; Croft, M.; Ignatov, A.; Sun, J.; Greenblatt, M. *Chem. Sci.* **2010**, *1*, 751–762.
- (39) Heald, S. M.; DiMarzio, D.; Croft, M.; Hegde, M. S.; Li, S.; Greenblatt, M. *Phys. Rev. B* **1989**, *40*, 8828–8833.
- (40) Liu, X. J.; Matsuda, K.; Moritomo, Y.; Nakamura, A.; Kojima, N. *Phys. Rev. B* **1999**, *59*, 7925–7930.
- (41) Liu, X. J.; Moritomo, Y. *Chin. Phys. Lett.* **2003**, *20*, 2027–2029.
- (42) Kresse, G.; Furthmüller, J. *Comput. Mater. Sci.* **1996**, *6*, 15–50.
- (43) Perdew, J. P.; Burke, K.; Ernzerhof, M. *Phys. Rev. Lett.* **1996**, *77*, 3865–3868.
- (44) Krukau, A. V.; Vydrov, O. A.; Izmaylov, A. F.; Scuseria, G. E. *J. Chem. Phys.* **2006**, *125*, 224106.